Emergence of ion-channel mediated electrical oscillations in *Escherichia coli* biofilms.

Emmanuel U. Akabuogu[1,2], Victor Martorelli[1,2], Rok Krašovec[3], Ian S. Roberts[1*], Thomas A. Waigh[2+]

Abstract

Bacterial biofilms are communities of bacteria usually attached to solid strata and often differentiated into complex structures. Communication across biofilms has been shown to involve chemical signaling and, more recently, electrical signaling in Gram positive biofilms. We report for the first time, community-level synchronized membrane potential dynamics in three-dimensional *E. coli* biofilms. Two hyperpolarization events are observed in response to light stress. The first requires mechanically sensitive ion channels (MscK, MscL and MscS) and the second needs the Kch-potassium channel. The channels mediated both local spiking of single *E. coli* biofilms and long-range coordinated electrical signaling in *E. coli* biofilms. The electrical phenomena are explained using Hodgkin-Huxley and 3D fire-diffuse-fire agent-based models. These data demonstrate that electrical wavefronts based on potassium ions are a mechanism by which signaling occurs in Gram negative biofilms and as such may represent a conserved mechanism for communication across biofilms.

*i.s.roberts@manchester.ac.uk

+t.a.waigh@manchester.ac.uk

[1]Division of Infection, Lydia Becker Institute of Immunology and Inflammation, School of Biological Sciences, University of Manchester, Oxford Rd., M13 9PT, UK.

[2]Biological Physics, Department of Physics and Astronomy, University of Manchester, Oxford Rd., Manchester, M13 9PL, UK.

[3]Division of Evolution, Infection and Genomics, School of Biological Sciences, Faculty of Biology, Medicine and Health University of Manchester, M13 9PT, UK.

Keywords: *E. coli*, biofilm, Kch, bacteria, electrophysiology, ion channel

Introduction

Dense microbial communities attached to surfaces are classified as biofilms[1]. Biofilms account for ~80% of chronic infections and are costly to eradicate in medical applications[2]. Bacteria in biofilms have recently been found to modulate their membrane potentials similar to excitable eukaryotic cells[3 4]. Potassium ion-channel-linked electrical signalling was first characterized in Gram-positive *Bacillus subtilis* biofilms[3]. It enables communication in bacterial biofilms due to the transmission of potassium wavefronts in the local environment of the biofilm. The potassium wavefront occurs in both centripetal and centrifugal varieties[5] and emerges spontaneously after the biofilm has grown to a critical size[6]. Photodynamic therapy using blue light causes a process of stage-dependent cell dispersal in biofilms and membrane hyperpolarization[7]. Such therapy has thus been investigated in detail for the treatment of topical infections[8,9] .

Membrane potential dynamics in prokaryotes are orchestrated using ion-channels. Gating of these channels can be controlled by voltage changes, heat, light stress, metabolic stress, mechanical stress and chemical agents[3,10–13]. In *B. subtilis* biofilms, only the potassium ion channel, *YugO*, has been directly linked to electrical signaling [3].

To date, robust ion-channel mediated signalling in biofilms of Gram-negative bacteria has not been described. Gram-negative bacterial biofilms have higher resistance to antimicrobial molecules than Gram-positive bacterial biofilms[14,15]. Although voltage related spiking dynamics have been observed in single *E. coli* cells[15,16], only second long stochastic transients have been measured with no distinct coordination between intercellular spikes.

The Kch potassium ion channel in *E. coli* was discovered in *E. coli* by Milkman[17] using comparative genetic techniques. The current consensus is that Kch is a voltage-gated ion channel, although the evidence is slightly indirect[18,19]. The current study provides additional evidence for the voltage-gated nature of the Kch channel in *E. coli* and indicates a physiological role for the ion channel.

We studied three-dimensional ion-channel mediated signalling in *E. coli* biofilms. We found that under light stress, *E. coli* hyperpolarize twice in response to continued light radiation. We hypothesize that the first peak is when *E. coli* first register the presence of an external stress in their vicinity and appears to be mediated by mechanosensitive ion channels. The depolarization and subsequent second peak that occurs in response to continued stimulation corresponds to a habituation phenomenon and is dependent on the Kch potassium gated channel. On the basis of these data we devised models (Hodgkin-Huxley and 3D fire-diffuse-fire agent based models) that

explain ion channel mediated signalling in *E. coli* biofilms. The work provides a novel outlook on the emergent electrophysiology of bacterial biofilms.

Results

Blue light triggers electrical spiking in single *E. coli* cells

We exposed *E. coli* (DH5α) to a blue LED (Fig 1A). Single sparse cells are defined as those with no neighboring cells within 10 µm. We monitored the membrane potential dynamics with the cationic fluorescent dye, Thioflavin (ThT)[20]. ThT is a Nernstian voltage indicator[21] which accumulates because bacterial cells have negative potentials[7,22,23]. We observed a cell-wide rise in the intensity of fluorescence, a period of quiescence followed by a slow increase in intensity which persisted until the end of the 60-minute experiments (Fig 1B, Video S1). Applying the blue light for different time periods and over different timescales yielded no change in the number of peaks (supplementary Fig 1A). We confirmed that this spike profile existed in other *E. coli* strains (*E. coli* BW25113, supplementary Fig 1B) and was also detectable when *E. coli* cells were grown in Minimal (M9) media (supplementary Fig 1C).

We observed similar spiking dynamics when we employed the lipophilic cationic cell permeant membrane potential dye, tetramethyl rhodamine methyl ester (TMRM) (supplementary Fig 1D). We then tested if the observed dynamics is related to the membrane potential or autofluorescence. We used carbonyl cyanide m-chlorophenyl hydrazone (CCCP) which rapidly quenches membrane potential related dynamics in *E. coli*[13,16,24]. When CCCP was added, no spiking dynamics (supplementary Fig 1E), confirming that the observed dynamics is membrane potential related.

Membrane potential dynamics depend on the intercellular distance

We hypothesized that the time-to-first peak latency of cells in dense microclusters of *E. coli* could differ from that of sparse single *E. coli* cells. A microcluster is defined as a cell community in which intercellular distances do not exceed two cellular diameters (Fig 1 C). We applied the same light stimuli as before to *E. coli* DH5α microclusters. We observed a rapid rise in intensity, a decay and subsequently a persisting second peak (Fig 1D, Video S2). The analysis of time-to-first peak latencies in sparse and microclustered cells showed that the average time-to-first peak was 7.34 ± 10.89 ± 4.44 min (*mean* ± *SD* ± *SE*) and 3.24 ± 1.77 ± 0.53 min (*mean* ± *SD* ± *SE*) (Fig 1E) respectively. The membrane potential dynamics of single cells showed more variability in spikes and less synchrony in the phases of the first spikes than those in microclusters (Fig 1B, Fig 1D). This suggests that random electrical signaling in *E. coli* synchronizes as the cells become clustered. We would

expect that mutual shielding from the light at higher cell densities should decrease the irradiance that cells experience which should increase the reaction time of the bacteria, however, in our experiments the opposite is observed. We also confirmed that 10 µM of ThT does not affect the growth of the *E. coli* strains used in the experiment (Fig 1F).

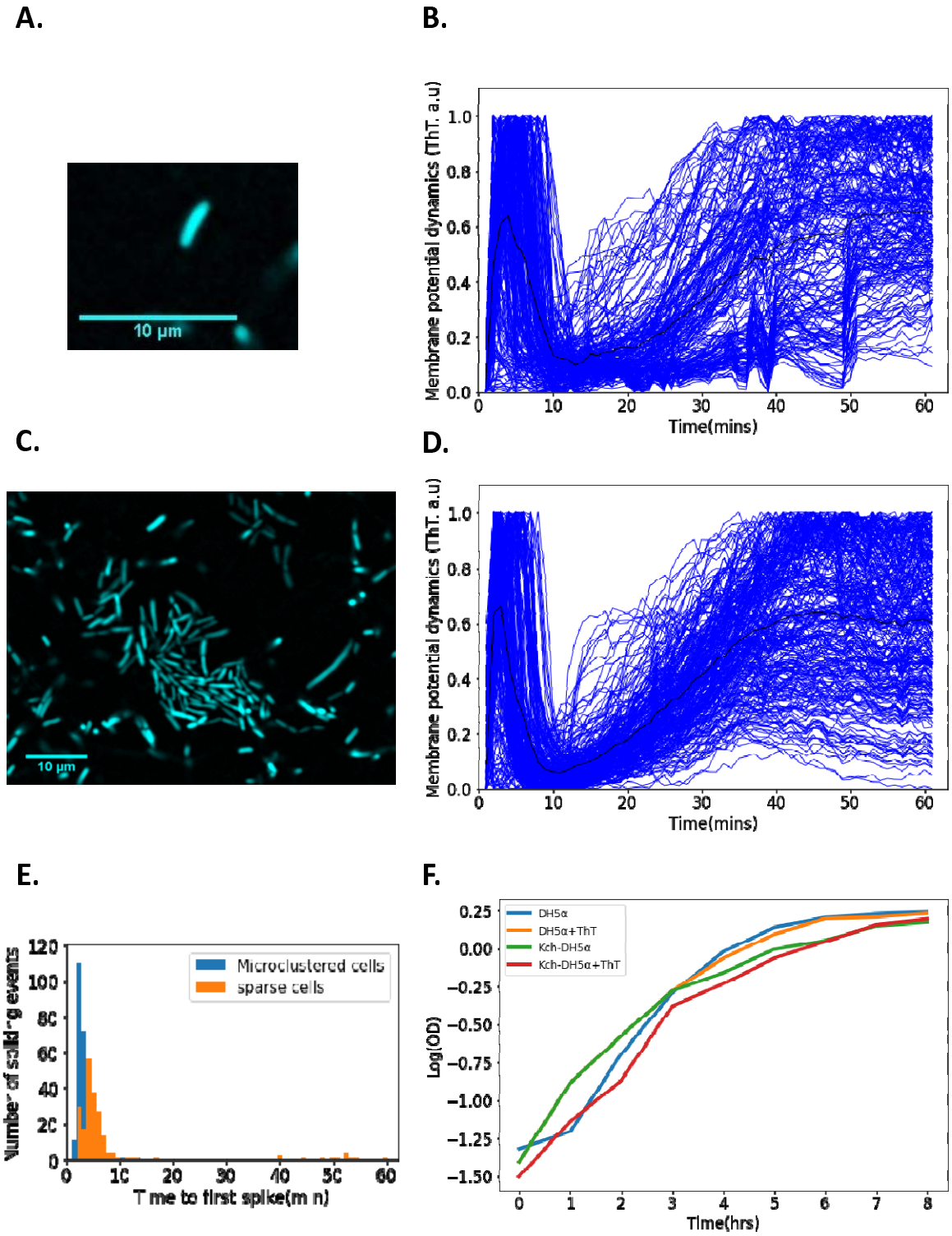

Figure 1. Single cell DH5α *E. coli* exhibit membrane potential dynamics in response to 440 nm blue light stress. (A) Image of a sparse single cell containing ThT imaged in the microfluidic device (Scale bar: 10 µm). (B) Normalized fluorescence intensities of ion-transients for sparse cells (n = 206) as a function of time after stimulation. Each curve describes a single cell. The curve depicting the mean membrane potential dynamics is shown in black. (C) Representative image of microclustered cells containing ThT in the microfluidic device. (D) Fluorescent intensity of ion-transients for cells in microclusters as a function of time after stimulation. Each curve describes a single cell. The curve depicting the mean membrane potential dynamics is shown in black. (E) Time to first spike histogram for sparse cells (n = 206, Sparse cells in orange) and cells in microclusters (n=272, microclustered cells in blue, cells recovered from 15 clusters). The number of spiking events is shown as a function of time to the first spike. (F) Growth curves (in a semi-log coordinates) for *E. coli* (measured via OD_{600}) as a function of time in the presence and absence of ThT. All data were from at least three experimental replicates. Light stress was applied for 60 minutes. The scale bars for all the images are 10 µm.

Emergence of synchronized global wavefronts in *E. coli* biofilms

A microfluidic chamber (supplementary Figs. 2A, 2B, Microfluidic section in Methods) was used to explore the growth of *E. coli* from single cells into biofilms (Fig 2A, supplementary Fig 3A)[3,7]. We exposed our biofilm to blue light. We observed a spontaneous rapid rise in spikes within cells in the center of the biofilm while cells at the periphery remained significantly less bright (Fig 2A, 2B, Video S3). The ion-channel mediated wave fronts moved from the center of the biofilm to the edges. At this point, the whole biofilm had an equal level of fluorescence intensity. The wavefronts then rapidly collapsed from the edges to the center of the biofilm. Once the wavefront reached the center, the whole system engaged in a period of quiescence and remained dark even in the presence of the continued external light stimulation. After a few minutes of inactivity, the wavefront reemerged from the center of the biofilm and slowly reached the periphery of the biofilm. After reaching the edges for the second time, the hyperpolarization persisted, and the entire biofilm remained bright and showed no noticeable change in response to the continued presence of the external stimuli. The latency of the first peak was 2.73 ± 0.85 ± 0.15 min (*mean* ± *SD* ± *SE*). This was a smaller period than that of cells in microclusters and sparse cells (Figs 1B and 1D, supplementary Fig. 3B). Furthermore, the variability of the latency (*SD*) was much lower.

Biofilms of different shapes and sizes were grown and we observed similar intensity profiles for all the biofilms (Fig. 2C). The peaks of the spiking profiles in all the biofilms (Fig. 2C) show that the amplitude of the action potentials does not depend on the size of the biofilm. Consequently, we focused our analyses on time-related properties of the wavefront profiles. Action potentials in eukaryotic organisms are stereotyped events; therefore, the time-dependent properties of the spikes carry the information about the amplitudes of external stimuli[25]. The intensity profile of different biofilms across several experiments shows that the wavefront dynamics is robust once the biofilm has an appreciable size (Fig. 2C). These data provide evidence that coordinated signalling

directs ion-channel mediated wavefronts in *E. coli* biofilms. This data suggests that *E. coli* biofilms use electrical signalling to coordinate long-range responses to light stress.

A

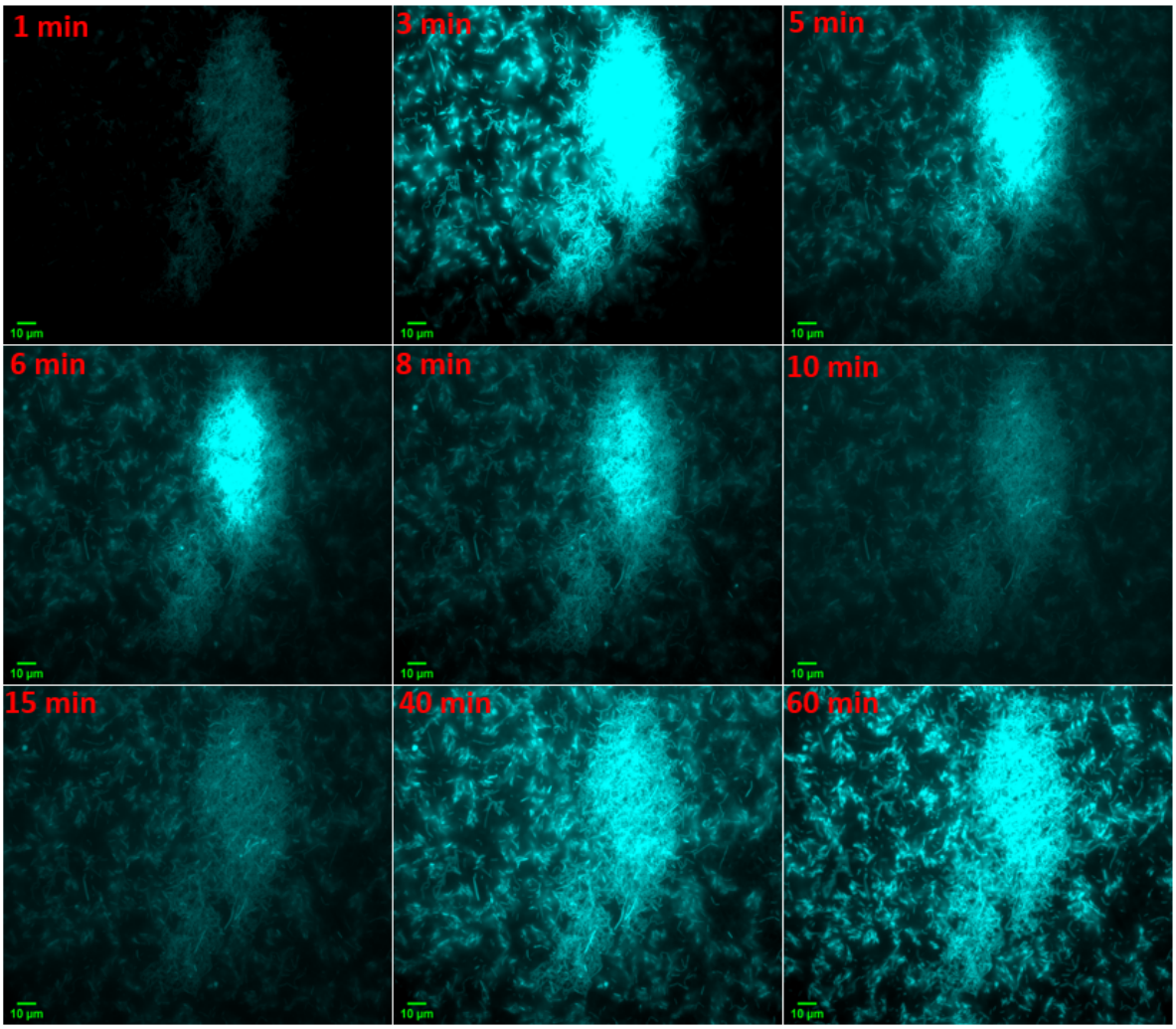

B

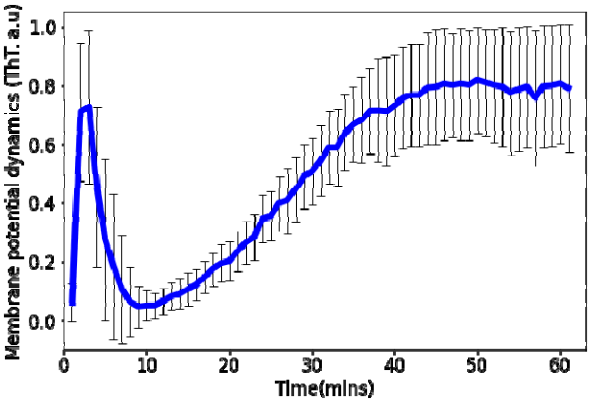

C

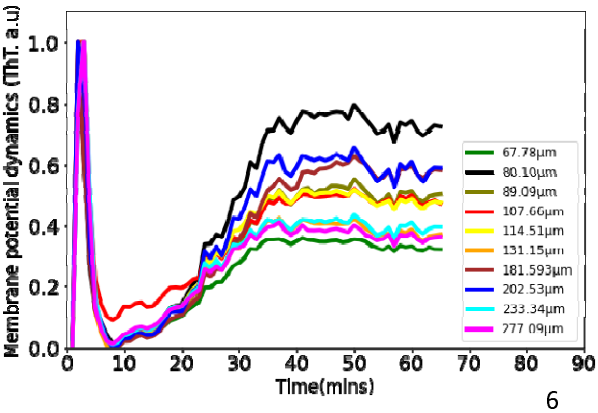

Figure 2: **Synchronized ion-channel mediated wavefronts in *E. coli* biofilm:** (A) Representative fluorescence microscopy image as a function of time (1-62 min). Robust global wavefronts can be seen in an *E. coli* biofilm with ThT. The scale bars for all the images are 10 µm. (B) Global averaged intensity trace obtained from a 2D section of a biofilm as a function of time (*mean* ± *SD* for 30 biofilms from at least 3 experiments). (C) Globally averaged ion-channel mediated dynamics in *E. coli* biofilms for different sized biofilms (68-277 µm). ThT intensity is shown as a function of time.

Voltage-gated Kch potassium channels mediate ion-channel electrical oscillations in *E. coli*

We hypothesized that the potassium channel, Kch[26], mediates the ion-channel membrane potential dynamics in *E. coli*. This ion channel (Fig. 3A) helps *E. coli* to survive environmental stress[27], but its deletion does not impede the development of *E. coli* from single cells into biofilms[27,28]. Kch had not been previously linked to action potentials and electrical signaling in *E. coli* biofilms[18,19].

We applied light stimulation to a Δ*kch* mutant of strain BW25113 from the Keio collection[29] and saw a fast burst of membrane hyperpolarization identical to the wild-type, but there was a plateau that remained for the whole duration of the experiment (supplementary Fig 3C, Video S4). There was no repolarization or slow rise to the second peak seen in the wildtype (Fig 1B and 1D). This suggests that the K^+ ion channel Kch plays a role in the refractoriness and habituation of the dynamics but does not control the initial hyperpolarization event. Using P1-phage transduction, we moved the *kch* mutation into strain DH5α and confirmed the phenotype with the first peak but no second peak (Fig 3B and 3C, Video S4). These data showed that Kch potassium ion channels are important for electrical signaling in *E. coli* in the presence of blue light stress.

To validate the importance of the Kch channel in the membrane potential dynamics of *E. coli*, we complemented the *kch* mutation by introducing a plasmid that carries a cloned functional kch gene into strain Δ*kch*-DH5α. The *kch* complemented strain displayed the same membrane potential dynamics (supplementary Fig 3D) observed in the wildtype (Fig 1B, 1D). However, the quiescence period in our *kch* complemented strain was reduced compared with the wildtype, presumably due to an increased degree of expression of the *kch* gene on a multi-copy plasmid.

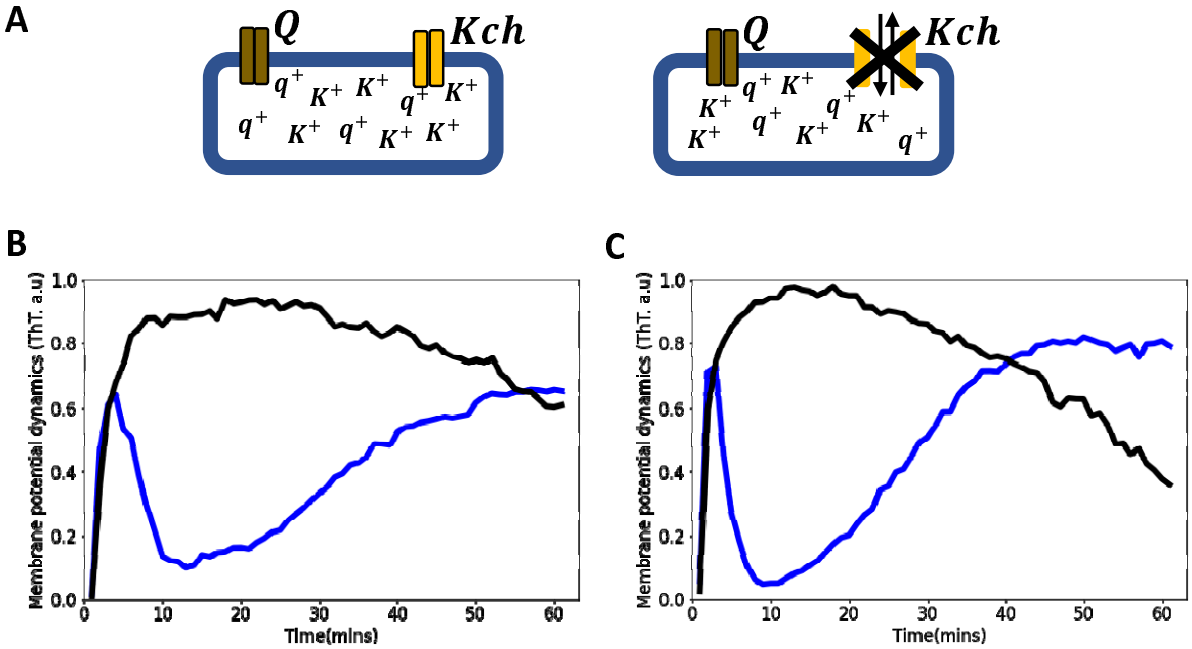

Figure 3. Voltage-gated Kch potassium channel mediates ion channel membrane potential dynamics in *E. coli.* (A) Schematic diagram showing the deletion of the voltage-gated *Kch* channel in *E. coli.* (B) ThT fluorescence shown as a function of time of irradiation. Deletion of *Kch* inactivates the second peak in *single cell E. coli* DH5α. Data is a mean from 52 single cells from three experimental replicates per time point for DH5α Δ*kch* mutant (black) plotted against the wildtype *single cell E. coli* DH5α (blue). (C) Deletion of *kch* also inactivates the second peak in *E. coli biofilms.* Data is shown for global membrane potential dynamics for biofilms grown from *E. coli* DH5α Δ*kch* mutant (black) and wildtype DH5α (blue).

Blue light influences ion-channel mediated membrane potential events in *E. coli*

To investigate the effect of irradiance on ion-channel mediated signalling, biofilms were exposed to blue LED light at different irradiances (Fig 4A). For all the irradiances we observed a first peak in the ThT fluorescence (Fig 4A). The time to the first peak decreased as the light irradiance was increased (Fig 4B). The fast burst of hyperpolarization and repolarization only occurred above the threshold of 15.99 μW/mm^2. For irradiances above this threshold, the dynamics exhibited progressively faster hyperpolarization to the second peak with increased light, which was not observed for irradiances below the threshold.

We thereafter examined the extracellular changes in the potassium ion, K^+ ions, within regions close to biofilms. We used the yellow-green fluorescent potassium (K^+) indicator, ION potassium Green-4 (IPG-4), which can track changes in extracellular concentrations of potassium. We observed a sharp rise, a quiescence period and then a plateau similar to that of the ThT dynamics (Fig. 4C). This suggests that K^+ ions play a vital role in the observed membrane potential dynamics of the biofilm.

We validated our model with a LiveDead assay on the wildtype *E. coli* DH5α and a DH5α Δ*kch* mutant. Viable cells were monitored using propidium iodide (PI) (Material and Methods). Damaged cells appear red and we observed that 1.7% of cells stained red after 60 minutes of light exposure for the DH5α (Fig. 4D(1)) and 7.6% for the DH5α Δ*kch* mutant (Fig. 4D(2)). Student t-test showed that blue light stress damage to the kch-mutant is significant when compared with the DH5α (Fig. 4E). This data shows that wildtype DH5α cells which engage in full membrane potential dynamics better withstand the light stress and have lower lethal damage.

We used the ROS scavenger, catalase, to accelerate the removal of ROS. After the addition of the catalase, cells only registered the presence of the light (via the first peak), but aborted the process of repolarization, so the second hyperpolarization event does not occur (Fig 4F, Video S5). This demonstrates that the ion-channel mediated membrane potential dynamics is a light stress relief process.

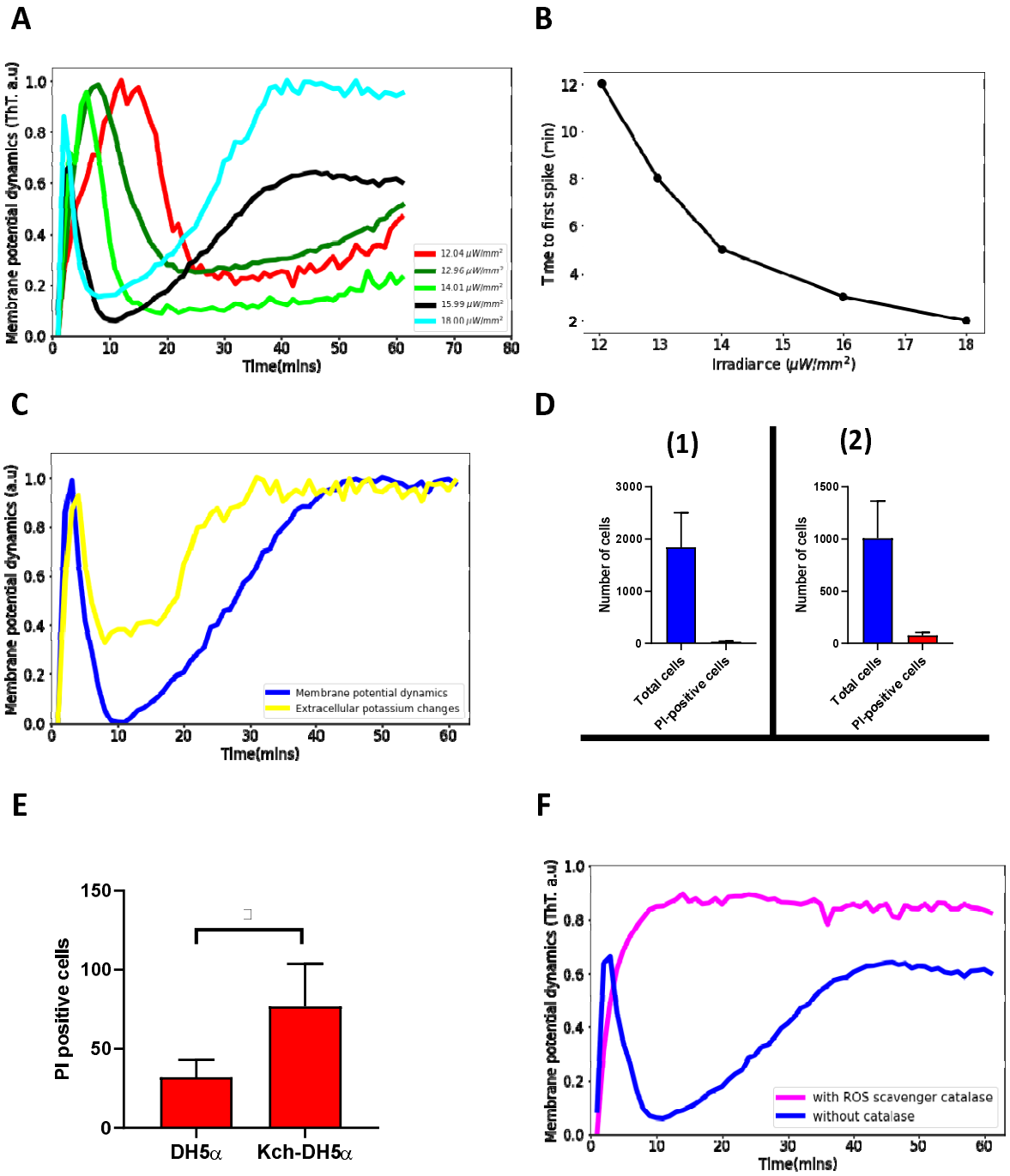

Figure 4. Blue light influences ion-channel mediated membrane potential events in *E. coli.* (A) ThT intensity as a function of time when irradiated with different powers of 440 nm light. The time to the second excitation peak is dependent on the power. All subsequent experiments were done at the irradiance value of 15.99 μW/mm^2. (B) Time to first spike plotted as a function of irradiance. Blue-light irradiance affects the time to the first peak in *E. coli* biofilm. (C) Measurement of extracellular potassium changes for regions close to biofilms as

a function of time using fluorescence microscopy. (D) LiveDead Assay using the accumulation of propidium iodide in cells (1) DH5α (n= 1842) (2) DH5α Δ*kch* mutant (n= 1008). (E) Comparison between PI positive cells for the DH5α and the DH5α Δ*kch* mutant. Statistical significance was calculated using the Student's t-test. * $p \leq 0.05$. (F) ThT fluorescence intensity as a function of time for cells in the presence of a ROS scavenger. *E. coli* cells employ ion-channel mediated dynamics to manage ROS-induced stress linked to light irradiation. Data was obtained from not less than three experiments.

Development of a Hodgkin-Huxley model for the observed membrane potential dynamics in single cells

Our data provide evidence that *E. coli* manages light stress through well-controlled modulation of its membrane potential dynamics. The light-induced ion-channel mediated dynamics present at the single cell level become more coordinated at the biofilm level (supplementary video S1 and S3).

To understand the biophysical mechanism of the ion channel opening for a single cell, we developed an electrophysiological model. Our Hodgkin-Huxley conductance model predicts that the membrane potential dynamics in *E. coli* biofilms are due to cooperative signaling between two distinct positively charged ion channels (Q and Kch) whose conductivities are voltage gated. We propose that the dynamics causes a process of long-range electrical communication of light stress in the *E. coli* biofilm. We also propose that the source of the photooxidative stress was due to increasing reactive oxygen species (ROS) in the vicinity of cells which gradually builds up as the light stress persists.

We predicted that the ion-channels activate and deactivate differently under the light stress (Fig. 5A,5B). Ion channel Q activates faster than the Kch channel, but deactivates slower than the Kch channel. Hence, while the Q channel activation dynamics is more pronounced for the sharp spike of the first peak, the Kch channel controls its subsequent decay. After the first action potential, the Q channel inactivates and contributes minimally to the dynamics. The Kch ion channel then controls the slow refractoriness and plateau which persists for a longer period in the presence of constant light stress (Fig 5B). This prediction supports our results from the deletion of the Kch ion channel from *E. coli* strains (Fig 3).

Our two ion-channel electrophysiological model correctly produced the same profile (Fig. 5C) as the experimental data (Fig. 5D). This model also predicts that the two spikes perform different roles in *E. coli*. The first spike registers the presence of light stress in the environment, while the second spike modulates the light stress by keeping the cell dynamics robust to the intensity of the external light stress. This mode of signaling is like a specialized type of electrical signaling in neurons called *habituation* (Figs 6A,6B). Sensory neurons can engage in signal

habituation to remain unresponsive to an external unwanted signal in the environment and still engage in control of other stimuli[30–32]. The model also predicts that the opening of the ion channels creates an increased concentration level of the extracellular ions which subsequently results in the depolarization of neighboring cells[13,33,34].

We hypothesized that *E. coli* not only modulates the light-induced stress but also handles the increase of the ROS by adjusting the profile of the membrane potential dynamics. We therefore varied the ROS stress production coefficient at different levels of light in the model. We observed a noticeable change in the membrane potential dynamics. With reduced ROS, the first spike became sharper and the quiescent time lasted longer than previously, with the second peak occurring at much higher intensities of light. With increased ROS, the first spike lasted less than 30 seconds and the 2nd spike plateau rose to a much higher fluorescence value. This result agrees with our hypothesis and further authenticates the involvement of two channels in the membrane potential dynamics of *E. coli.*

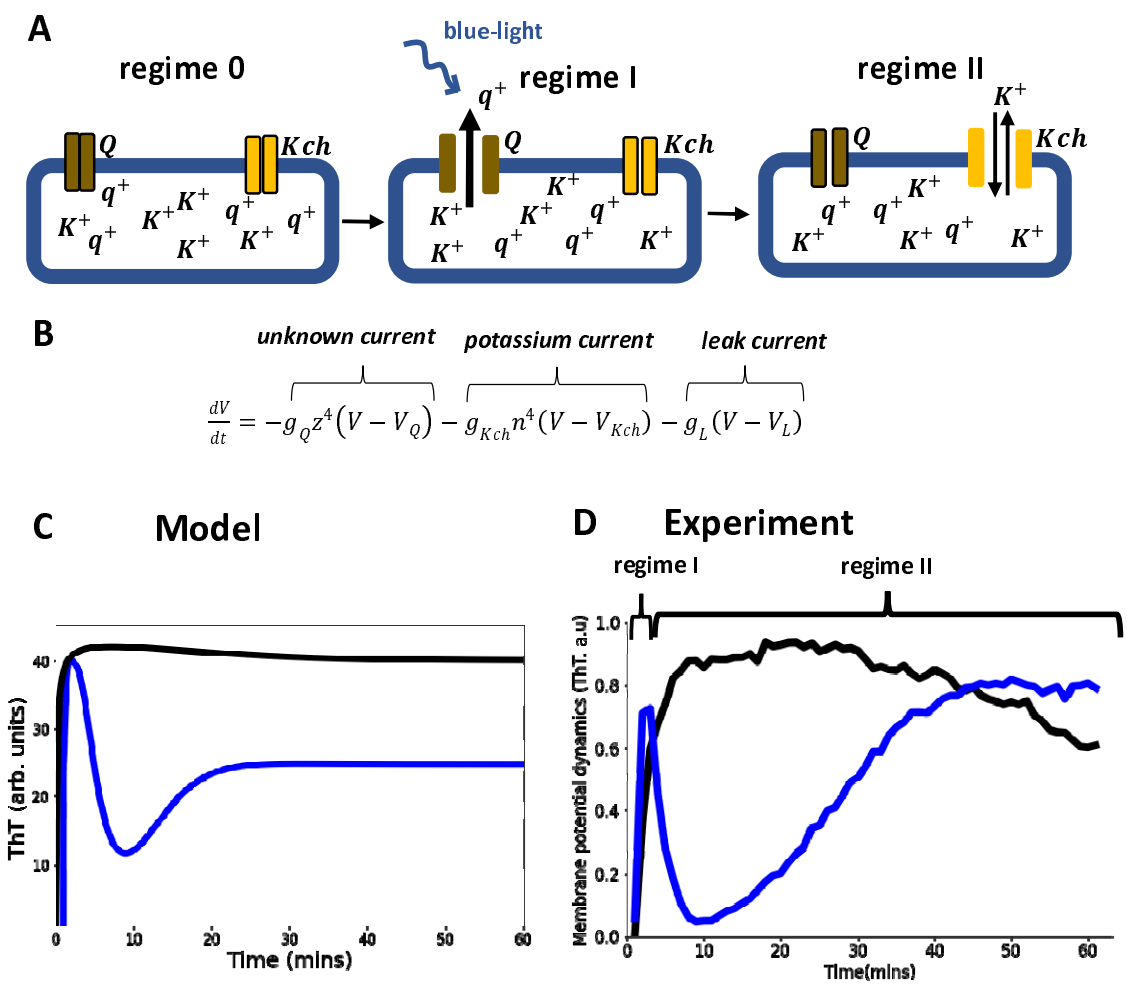

Figure 5. Model of ion-channel mediated membrane potential in *E. coli*, predictions and experimental validation. (A) Schematic diagram of the conductance model and its predictions. The model consists of two ion-channel gates. The first channel (bronze, Q) is unknown. The second channel is the potassium channel, Kch (yellow). At the onset regime 0, both ion channels are closed. Exposure to light stress results in a rapid opening of the *Q* channel, which has a faster-opening gating variable than the Kch channel (regime I). The *Q* channel has little contribution to the repolarization event, hence the overlap of regimes I and II (the blue light is present for both regimes). (B) In the Hodgkin Huxley type conductance model the current changes are modulated by the two ion channels (*Q* and *Kch*) and the leakage channel (*L*). (C) The predicted ThT fluorescence intensity as a function of time for the Hodgkin Huxley model. Our Hodgkin Huxley model correctly reproduces the *E. coli* membrane potential dynamics for the wildtype (blue) and kch-mutants (black). The wildtype has two hyperpolarization events. (D) Fluorescence intensity from our microscopy experiments with ThT as a function of time for the wildtype (blue) and *Kch*-mutants (black).

Mechanosensitive ion channels (MS) are vital for the first hyperpolarization event in *E. coli*.

We hypothesized that the first hyperpolarization event is linked to the voltage-gated calcium channels (VGCCs), so we introduced the fluorescent calcium sensor, GCAM6f[15] on a plasmid into the wildtype DH5α strain. When exposed to light stimulation, the spike events observed were consistent with stress-induced signaling of the VGCCs[10,15]. However, the calcium transients imply that the VGCCs (supplementary Fig 3E) do not play a role in the first peak of the *E. coli* strain under light stress (Figs. 1B,1D,2B).

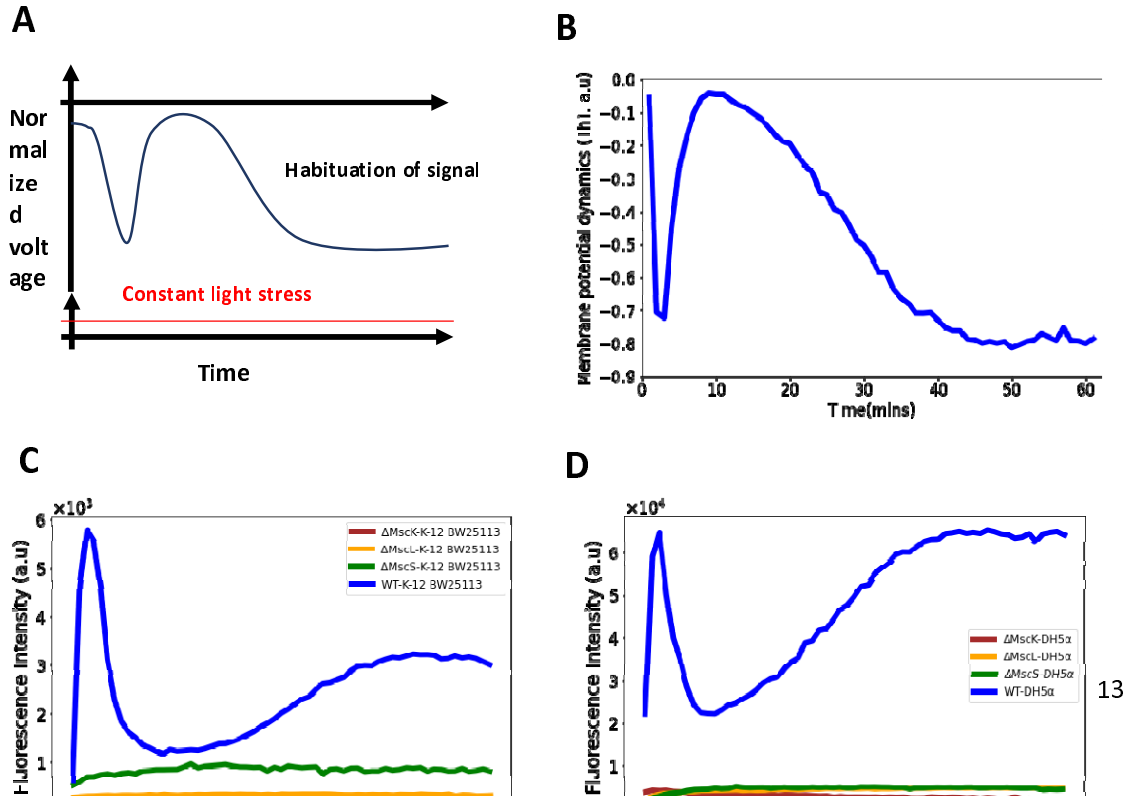

Figure 6. Role of mechananosensitive channels in the first hyperpolarization event in *E. coli*. (A) A generic diagram for the membrane voltage during neuronal habituation to a constant stimulus e.g light stress[31,32]. (B) An illustrative diagram of membrane potential dynamics of our experiment as a function of time which is a mirror image of the ThT dynamics for comparison with (A). (C) Membrane potential dynamics for MS mutants of the wildtype, *E. coli* strain BW25113. (D) Membrane potential dynamics for MS mutants of the wildtype, *E. coli* DH5α.

The mechanosensitive (MS) ion channels help maintain turgor pressure and are also sensitive to stress-related voltage changes[35–39]. We tested whether the MS ion channels in *E. coli*, MscK, MscL and MscS, play a role in the first spike of the membrane potential dynamics (Figs 1B, 1D, 2B). We exposed the mutant strains, Δ*MscK*, Δ*MscS* and Δ*MscL* of the wildtype, *E. coli* BW25113 (Fig 6C), to light stimulation and observed no spike dynamics typically observed with the wildtype cells (Figs 1B, 1D, 2B). Using P1-phage transduction, we transferred the mechanosensitive channel mutations into the strain DH5α and confirmed the phenotype (Fig. 6D).

Anomalous ion-channel-mediated wavefronts propagate light stress signals in 3D *E. coli* biofilms

We developed a 3D agent-based fire-diffuse-fire model (ABFDF) using BSim[40]. No analytical solutions are known for the FDF model in 3D, so simulations using agent-based models were needed. In our simulated 3D spherical biofilm (Fig 7A), we observed global membrane potential dynamics (Fig 7B, Video S6A) that are like our experimental data (Fig 2B).

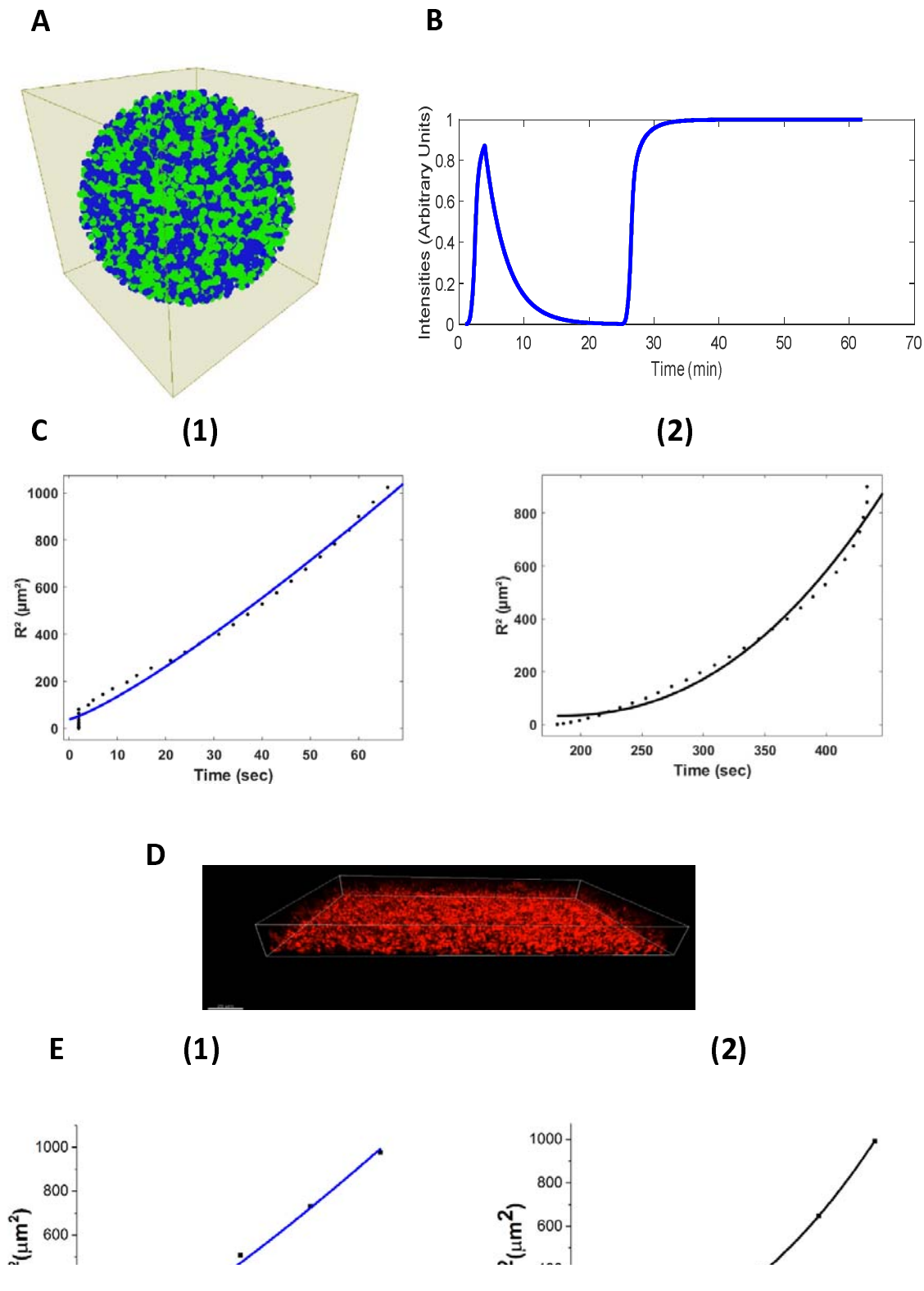

Figure 7. Agent-based Fire diffuse fire model (ABFDF) and experimental validation of anomalous ion-channel mediated wave propagation in three-dimensional *E. coli* biofilm. A) 3D spherical biofilm in a fluid-filled environment simulated using BSim. B) ABFDF global electrical signaling wavefront profile averaged over a three-dimensional biofilm. The ThT intensity is predicted as a function of time. C) Plot of the square radial distance of the wave front (R^2) against time and fit with a power law, $R(t)^2 = R_c^2 + bt^\gamma$. For the first peak's (1) centrifugal motion: $\gamma = 1.21 \pm 0.12$ and (2) centripetal motion: $\gamma = 2.26 \pm 0.31$ from ABFDF simulation data. D) Representative confocal fluorescence image for a sessile 3D biofilm with ThT (Scale bar = 20 µm). E) Plot of R^2 against time fit with a power law, $R(t)^2 = R_c^2 + bt^\gamma$ for the first peak's (1) centrifugal motion: $\gamma = 1.22 \pm 0.15$ and (2) centripetal motion: $\gamma = 2.43 \pm 0.08$ from the experimental data.

To understand the nature of the wavefront motion in the two phases of the first peak (outward followed by inward motion), the relationship between the radial distance and the time was determined. Fig. 7C shows the square radial displacement versus time. Data were fitted with power laws,

$$R(t)^2 = R_c^2 + bt^\gamma \quad , \tag{1}$$

where $R(t)^2$ is the square radial distance of the wavefront, R_c is the critical biofilm size for wavefront initiation, t is the time, b is a constant and γ is the exponent. The exponent γ describes whether the wave motion is *diffusive* ($\gamma = 1$), *subdiffusive* ($\gamma < 1$), *superdiffusive subballistic* ($1 < \gamma < 2$), *ballistic* ($\gamma = 2$) *or super-ballistic* ($\gamma > 2$)[41,42].

All ABFDF simulations produced superdiffusive subballistic behaviour for the wavefront from the core to the periphery (*centrifugal wave*) ($\gamma = 1.21 \pm 0.12$), whereas the periphery to the core (*centripetal wave*) was super-ballistic ($\gamma = 2.26 \pm 0.31$) (Fig 6C).

We experimentally tested these simulation findings using confocal microscopy and ThT. We grew a three-dimensional biofilm (126 µm x 172 µm x 31.8 µm) and exposed it to blue light (Fig. 7D). A timelapse of the sagittal section of the three-dimensional biofilm (supplementary Fig 4A) reveals membrane potential dynamic akin to the 2D projections through the biofilms (Fig 2A). The temporal membrane potential dynamics of the 3D biofilm (supplementary Fig 4B, Video S6B) was similar to our simulation results (Fig 7B).

Wave fronts propagating in three-dimensional systems emanating from a point source have a curved geometry[43]. We tested if the ion-channel wave propagates along the z-axis, adopting the z-plane analysis scheme[44–46]. Our experimental data (Fig. 7E) showed that the centrifugal wave is superdiffusive subballistic ($\gamma = 1.22 \pm 0.15$), while the wave motion for the centripetal wave is super-ballistic ($\gamma = 2.43 \pm 0.08$), in reasonable agreement with simulation. Furthermore, the results confirm that curvature affects the motion of the wavefronts[47]. Blee and co-workers[5] previously observed a superdiffusive wave motion for both the centrifugal ($\gamma = 1.42 \pm 0.06$) and centripetal phases ($\gamma = 1.79 \pm 0.03$) of the potassium wavefront in 2D *B. subtilis* biofilm. The centripetal wavefronts appear to travel faster than the centrifugal wavefronts.

Using eqn 1 we calculated the critical size for wave initiation in 3D *E. coli* biofilms from the experiments to be 4.71 ± 0.98 µm. This is reasonably close to the value predicted from our ABFDF model, 6.17 ± 1.84 µm. 3D *E. coli* biofilms, therefore, need to develop a densely packed biofilm above the critical radius for a robust synchronized ion-channel mediated wavefront to propagate in the system. This contrasts with 2D *B subtilis* biofilms which need to grow up to ~ 350 µm for a wavefront to emerge in the system[3,6,48]. Therefore, our model predicts the transport properties of the wavefront, the patterns of global excitation and the critical radius for wavefront propagation in biofilms (Table 1).

Table I. Fit constants for eqn 1 to results from the ABFDF and experimental data.

Constants	**Symbol**	**Centrifugal wavefront Model**	**Centripetal wavefront Model**	**Centrifugal wavefront Experiment**	**Centripetal wavefront Experiment**
The anomalous exponent	γ	1.21 ± 0.12	2.26 ± 0.31	1.22 ± 0.15	2.43 ± 0.08
The critical biofilm size	R_c	6.17 ± 1.84 µm	–	4.71 ± 0.98 µm	–

As expected, we observed a slow decrease of velocity as the wavefront spread from the core towards the periphery i.e. from the Eikonal approximation. The Eikonal approximation provides the relationship between the curvature and wavefront of a wave emanating from a source. For the velocity of the wavefront that travels back to the core, we observed a decrease and subsequently a sharp increase at distances close to the core of the biofilm (Figs. 8A and 8B). This unexpected behavior may be linked to the heterogeneity of microclusters within the bacterial biofilms. A

nonlinear relationship is also observed between the wavefront velocity and curvature for centrifugal and centripetal wavefronts (supplementary Fig 5 A, 5B and 5C)

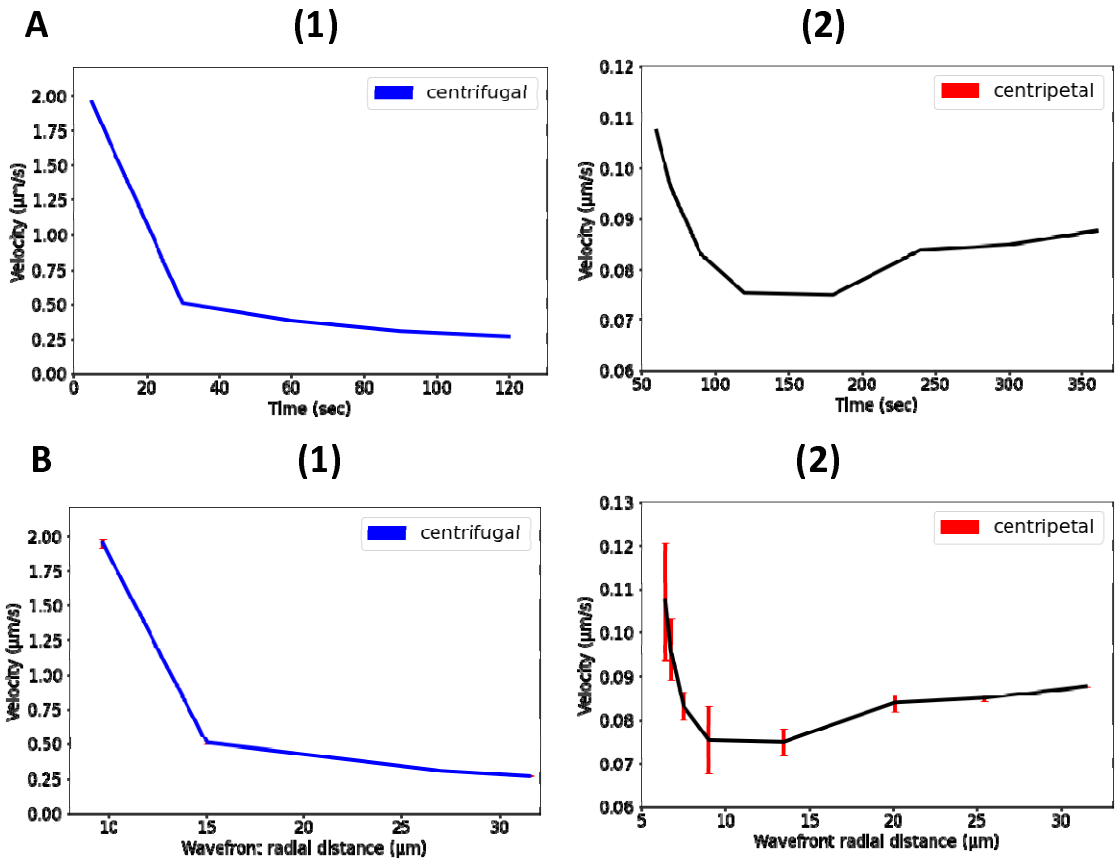

Fig 8. Nonlinear propagation of ion-channel mediated wave in 3D *E. coli* biofilms A) Nonlinear relationship between propagation velocity of the wavefront and the time for (1) centrifugal wave and (2) centripetal wave of the first peak. B) Nonlinear relationship between propagation velocity of the wavefront and the radial distance for (1) centrifugal wave and (2) centripetal wave of the first peak.

Discussion

E. coli biofilms synchronize ion-channel-mediated electrical signaling when under external light stress. The process of communicating the stress becomes faster as the intercellular distance decreases and it results in robust wavefront dynamics in which bacteria take turns to spike in a coordinated manner.

Our experimental data reveals that ion-channel-mediated wavefronts exist in 3D *E. coli* biofilms. 3D wavefronts exhibit anomalous diffusive behavior, which was well described by our 3D ABFDF model. The mode of propagation of the wavefronts was like that described for *B. subtilis* under nutrient stress[3]. However, noticeable differences are in the frequency of oscillations, the latency, the dimensionality of the system and the number of spikes (two hyperpolarization events with *E. coli*).

Although Kch was the first potassium channel to experience detailed structural work in *E. coli*[26], it has never been linked to membrane potential dynamics. Our findings establish that the Kch channel plays an important role in *E. coli* membrane potential dynamics. Specifically, the channels control the refractoriness and second peak of the membrane potential. These phases of the dynamics were correlated with light stress modulation in *E. coli* biofilm. We therefore predict that light-based *E. coli* biofilm treatments should be more effective if coupled with Kch targeting modalities.

Both of the two models developed, the Hodgkin-Huxley (HH) model and the fire-diffuse-fire agent based model, provided new physical insights to understand photodynamic therapy. The HH model satisfactorily describes the globally averaged dynamics of the membrane potential in response to blue light and indicated a minimal model containing at least two ion channels (*Q* and *Kch*) was necessary to describe the double spiking response to blue light irradiation. The fire-diffuse-fire agent based model could quantify the anomalous dynamics of the wavefront and predict the critical biofilm radius needed for wavefronts to propagate. Anomalous dynamics of wavefronts are not predicted by classical analytic solutions to reaction-diffusion equations and are thus a substantial advantage of the agent based modelling approach we followed[49]. Future extensions of the theoretical models will be to predict the form of the wavefronts as they propagate in more complex geometries e.g. through mushroom shaped biofilms and around microchannels which are known to occur with *E. coli* biofilms[50]. Research on cardiac infarctions have extensively studied the effects of dead non-signaling tissue on propagating electrochemical wavefronts[49] to understand the effects of drug treatments on the pumping of the diseased heart. It would be interesting to consider the analogous system for electrical signaling in biofilms e.g biofilms with defect structures due to inanimate inclusions or mixed species biofilms.

Our data shows that the unknown ion channel (Q) is not connected to calcium dynamics, but it is connected with the mechanosensitive ion channels that work in tandem to propagate the initial spike in *E. coli* under light stress. Minimally the model predicts $Q=MscK \times MscL \times MscS$, but the full dependence is probably more complex. The initial spike is key to registering the presence of the light stress. More work is needed to unravel the detailed molecular mechanism linking the MS channels and light stress gating in *E. coli*, but the data demonstrate a role for MS channels beyond osmo-protection.

When bacterial cells experience light-based stimulation, they experience stress which can be cytotoxic[51,52] due to the production of ROS. The accumulation of ROS leads to deleterious oxidative stress that damages molecules[51,53]. The propagation of action potentials in the presence of changing irradiance suggests that the stimulus strength is encoded in the response of the biofilms. The membrane potential dynamics also suggest a link between the duration of the stimulus, the oxidative stress due to the strength of the irradiance and the gating of the ion channels that modulate the dynamics.

The unresponsive nature of *E. coli* after the second hyperpolarization event and its marked plateau voltage is reminiscent of the phenomenon of signal habituation in neurons[54]. Neurons discriminate between external stimuli by observing a sustained decrement in response to a constant external stimulus[30–32]. *E. coli* biofilms mostly switch to a viable, but non-culturable phenotype when exposed to either pulsed or constant blue-light therapy[52,55,56]. We suggest that the habituation after light stress registration could be involved.

Our work shows that the ion-channel mediated long-range electrical membrane potential in *E. coli* biofilms help them to withstand light stress. We believe that our findings will provide a good framework for more detailed optogenetic studies of membrane potential signaling in *E. coli* biofilms and help inform photodynamic therapies to combat problematic biofilm infections.

Recent work indicates that waves of hyperpolarization also occur across biofilms of *N. gonorrhoeae*[57]; another example of electrophysiological phenomena in medically relevant biofilms. The signaling wavefronts were thought to be due to diffusion of ROS rather than the potassium ions observed with *E. coli* biofilms, but genetic experiments with ion channel mutants to clarify this issue were not performed. The *N. gonorrhoeae* study used an analytic reaction-diffusion model to describe the signaling phenomena. We have presented much better quantitative agreement of our model with the propagating wavefronts in *E. coli* biofilms using reaction-diffusion equations combined with agent based modelling e.g the ABM FDF model is able to predict the anomalous dynamics of the wavefronts and the critical biofilm size for propagation of the wavefront. Such agent

based modelling should be applied to *N. gonorrhoeae* biofilms in the future due to the better handling of geometric constraints in the models.

The electrophysiological properties of bacteria is a rapidly evolving area[58]. Connecting the membrane potential to photodynamic therapy implies there will be synergistic effects of externally applied electric fields and blue light on bacterial infections. Thus, conducting dressings could be combined with blue light to improve the efficacy of wound treatments[59]. Furthermore, recent experiments have connected antibiotic activity to fluctuating membrane potentials with *E. coli*[60]. This in turn implies that synergistic effects will occur between blue light and antibiotic treatment e.g more cationic antibiotics will be absorbed by cells that hyperpolarize in response to blue light and the performance of the antibiotics will be modulated by ion channel activity.

Methods

Bacterial Strains

The bacterial strains and the media recipes used in this study are listed in the Supplementary Table 4. All experiments were performed with the DH5α and BW25113 strains of *E. coli*. All other strains were derived from these two and are listed in Table 1, Materials and Methods. When genes were moved by transduction into DH5α the resulting mutations were sequenced to confirm authenticity.

Dyes and Concentrations

ThT was used at a final working concentration of 10 µM for both LB and M9 media. This is the concentration that did not inhibit bacterial cell growth or influence the voltage flux in previous experiments[3,7,34]. Fresh ThT was made up on the day of each experiment and added to the media containing the cells.

To measure extracellular potassium, the IPG-4 AM was converted to its membrane impermeable form. This was achieved by dissolving the dye in 250 µl DMSO and subsequent addition of 0.1M KOH.

CCCP and TMRM were used at the final concentrations of 100 µM and 100 nM respectively. Propidium iodide (PI) was used at a final concentration of 1 µg/ml.

Microfluidics Setup and Experimental Design

All microfluidic experiments were performed with IBIDI uncoated glass bottom µ-Slide VI$^{0.5}$ flow cells (Thistle Scientific, UK) which have dimensions of $17\,mm \times 3.8\,mm \times 0.54\,mm$ for the length, width and height respectively (Supplementary Fig 2A and 2B). The system yielded successful growth for all *E. coli* strains and allowed high-resolution microscopy images to be taken. Single cells and microclusters were also cultured in this system. The microfluidic components and software are listed in Supplementary Table 4.

Growth media (LB or M9) contained in a 20 ml syringe (BD Emerald, UK) were delivered to the microfluidic wells by an Aladdin NE-1002 Programmable Syringe Pump (World Precision Instruments, UK). The media was replenished at intervals throughout the experiment. A C-Flex laboratory tubing with I.D. x O.D. 1/32 in. x 3/32 in (Sigma-Aldrich) and Elbow Luer connector male (Thistle Scientific, UK) completed the microfluidic setup. A 0.22 µm filter was installed at the syringe hub before attaching the syringe needle 0.8 × 40 mm to maintain sterility and reduce the number of air bubbles. Exchangeable components of the microfluidic setup were used only once. Experiments were conducted in more than one channel at a time for data replicates. Prior to the start of the experiments, the flow cell chambers were primed with appropriate media to achieve faster cell attachment. The microscope and all the components of the microfluidic setup were confined within the custom-built Perspex microscope chamber which was maintained at 37^oC using an Air-THERM ATX (World Precision Instrument Ltd.).

For single cell experiments, cells were left static in the microfluidic chamber for 2 hours for cells to attach to the substrate. The media was then delivered at flow rates of 3 µL/min and subsequently maintained at 5 µL/min to remove unattached cells from the system. After 1 hour of media flow, data were only collected for cells that were attached to the substrate. For biofilms, the system was left static 2 - 3 hours on the microscope after loading to allow the cells attach. Media flow was initiated at the rate of 5 - 6 µL/min and maintained for a further ≈12 hours (see Time-lapse Microscopy section).

Cell culture and Growth conditions

(I) Single cell Culture

Cells were streaked onto an Agar plate from -80^oC glycerol stocks a day prior to the experiment and incubated at 37^oC overnight. The following day, 10 ml of Luria Broth (LB) in a glass universal bottle was inoculated with one colony of the required *E. coli* strain. The inoculum was then incubated overnight in a shaking incubator at 200 rpm at 37^oC. The next day, $10\,\mu l$ of the inoculum

was transferred to a fresh 10 ml LB and incubated in a shaking incubator at 200 rpm at 37^oC for 4.5 hours or $OD_{600} \approx 0.8$. The optical density of the cells was measured using a spectrometer (JENWAY, Cole-Parmer UK). $10\ \mu M$ ThT was added to the inoculum and left static for 20 minutes. $200\ \mu l$ of the cell suspensions were then seeded into the required chambers of the microfluidic device. The microfluidic device was mounted on the microscope after attaching the other microfluidic components, such as tubes and tube connectors. The instrument was left static for 2 hours to allow for cell attachment before the media was delivered under flow. To sustain the growth temperature at 37^oC, a custom-built Perspex microscope chamber heated using an Air-THERM ATX (World Precision Instrument Ltd.) was employed. The salts for the M9 media are listed in supplementary Table S4. Data were collected for both sparse cells and cells existing within microclusters. The single cell experiments were done in Luria Broth (LB) media and replicated in Minimal media (M9) (supplementary fig 1C) to demonstrate independence on the exact media used.

For the LiveDead Assay, the same protocol was followed. However, before seeding the well with 200 µL of the inoculum, 10 µL (1 µg/mL of the stock solution) of PI was added to the 10 ml universal bottle containing cells and ThT.

For the combined CCCP experiments, the same protocol was also followed. 100 µM of CCCP was introduced into the universal bottle containing inoculum and ThT. This was left for 50 minutes, then 200 µL of the suspension was transferred into the wells and cells were exposed to blue light stress.

(II) Biofilm Growth

The *E. coli* DH5α strain was chosen based on its ability to adhere to surfaces and to grow into biofilms [61–63]. Biofilms were grown in one of the chambers of the microfluidic devices. Single cell *E. coli* was cultured as described in section (I). 200 µL of bacteria culture suspensions with ThT were added and then loaded in the flow cell to initiate biofilm formation. The setup was left static for 2 hours within the microscope chamber before the media flow was initiated at a rate of 5 - 6 µL/min for a further 12 hours. Under sterile and constant media flow (explained in the Microfluidic section) to produce optimal growth conditions, sessile biofilms were observed. Our protocol was optimized to obtain sessile DH5α biofilm after 15 hours. The growth temperature was maintained at 37^oC using a custom-built Perspex microscope chamber heated using an Air-THERM ATX (World Precision Instrument Ltd.). Media replacement was done within the microscope chamber to maintain sterility and avoid air bubbles.

Time-lapse microscopy and image acquisition

Fluorescence microscopy was performed with an Olympus IX83 inverted microscope (Klaus Decon Vision) using Blue Lumencor LED excitation (illumination), a 60x (NA 1.42 Plan Apo N) oil immersion objective and the CFP filter set (Chroma [*89000*]). Time-lapse fluorescence images were taken with a Retiga R6 CCD camera [Q-imaging]. ThT fluorescence was measured in the CFP channel using an excitation filter (Ex) 440/20 nm and an emission filter (Em) 482/25. PI fluorescence was measured with the Ex 575/20 nm and Em 641/75 nm. Images were taken every 1 minute with an exposure time of 50 ms and camera gain of 3. Prior to setting up the microfluidic apparatus on the microscope, the chamber was maintained at $37^{o}C$ for at least 3 hours. Image acquisition on the PC was carried out using the MetaMorph software (Molecular devices). This microscope and the settings were used for all observations on single cells and 2D biofilms. The settings were varied for the irradiance experiment (see section on Irradiance measurement below). Images in supplementary fig. 1A were obtained at different time scales (every 10 seconds) for comparison. The pump was turned off before the image acquisition to minimize image drift and vibrations.

Fluorescence confocal 3D image stacks for the 3D biofilm were acquired using a CSU-X1 spinning disc confocal (Yokagowa) on a Zeiss Axio-Observer Z1 microscope with a 63x/ 1.40 Plan-Apochromat objective, Evolve EMCCD camera (Photometrics) and motorised XYZ stage (ASI). A 445 nm laser line was used for ThT excitation. The 445 nm laser was controlled using an AOTF through the Laserstack (Intelligent Imaging Innovations (3I)) allowing for rapid 'shuttering' of the laser and attenuation of the laser power. Slidebook software (3I) was used to capture images every 1 minute with 100 ms exposures. Movies were analysed in Slidebook, ImageJ and Imaris (bitplane) software.

Image and Data Analyses

ImageJ (National Institute of Health), MATLAB, BiofilmQ and Imaris (bitplane) software were used for image analysis. Data analyses and plots were done with Python, BiofilmQ and GraphPad (Prism). Python and Scipy package were used for mathematical modeling. Model curve fits were done with Python Scipy package and OriginPro

(i) Single cells

Single cell image analysis was conducted using ImageJ (National Institute of Health). Background subtraction was done using the 'ImageJ rolling ball' background plugin with radii of 8 - 11 µm. This was influenced by experimental conditions e.g media. An ImageJ custom script was used for drift correction. Data were plotted with standard deviations for the error bars. Data were normalized in python for final plotting.

For LiveDead assay experiments we used the imageJ plugin 'cell counter' to identify and count cells. Only cells that are hyperpolarized were counted in the experiment as live and only cells that appeared red after the experimental duration were counted as dead. Time to first peak analysis was done by measuring the individual times for each single cell to experience the first hyperpolarization event.

(ii) Biofilms

To overcome the challenges of diversity in structure and size of the biofilms obtained in our experiments, we conducted image analysis of sessile biofilms with BiofilmQ. BiofilmQ is a high throughput MATLAB-based image processing and analysis software designed for spatiotemporal studies of both 2D and 3D biofilms. A detailed description of BiofilmQ can be found Hartman et al., 2021[64]. It has been used in a number of recent of recent investigations of biofilm[65,66]. We were able to accurately obtain membrane potential dynamics of biofilms by tracking ThT traces within the entire biofilm (2D and 3D confocal stacks) using this software.

To ensure data reproducibility, we describe the individual steps in our analysis. The confocal image stacks were first prepared and registered before segmentation. Image preparation included colony separation to identify the preferred microcolonies within the ROI and image alignment was used to correct image drift over time. Image segmentation was then carried out to separate cells from the background. Specifically, image cropping was done to tag the microcolonies, this was followed by denoising of the image using convolutions. We opted not to use the top Hart filter because in our biofilms the cells overlap each other. A filter kernel value of [15 3] was employed for the convolution. This value of the filter kernel was used for all our data analysis. It was sufficient to only slightly blur the images and significantly reduce the image noise. To complete the segmentation process, we used the Otsu thresholding method. The sensitivity of the thresholding was set to 1 for all the biofilm analysis. We opted not to dissect the biofilm, since we were interested in the global membrane potential dynamics and ion-channel waves in the biofilms. These steps ensured reproducibility of our analysis across all the biofilms.

To verify the accuracy of this software, we also measured the temporal dynamics of the membrane potential by tracking the global ThT fluorescence of biofilms using ImageJ. To obtain ThT curves in imageJ, we used the 'plot-Z axis' function on the imageJ image analysis toolbox. This has been used

in previous research work to successfully track the biofilm ThT fluorescence [3,5]. We confirmed that BiofilmQ was efficient for our data analysis.

The optical sections for the velocity measurements were obtained with a combination of both the BiofilmQ and IMARIS software. Radial distances of biofilm volumes from the substrate to the core of the biofilm were made with both BiofilmQ and IMARIS. The choice of the appropriate optical sections perpendicular to the z-slices were also made by the combination of both software.

440nm and 445nm Light Stimulation

E. coli cells and biofilms were treated with blue light using an Olympus IX83 440nm-LED and 445 nm laser line. The cells were exposed to the light every 1 minute. Experiments were performed with at least three biological replicates.

Irradiance Measurements

Irradiance experiments were conducted with the Olympus IX83 440nm-LED. Therefore, the irradiance was varied to ascertain the effect of the light stimulation on the membrane potential dynamics of *E. coli.* A Newport power/energy meter (Newport Corporation Irvine US) was used for the irradiance measurements. The power of the 440 nm light was varied by adjusting the percentage light illumination via the CFP light, e.g. 175 of the 255CFP that corresponds to $2.43\ \mu W$ as measured with the power meter. Uniform illumination of the sample ROI was always maintained via Köhler illumination.

To determine the irradiance, we first measured the power of the LED light at the sample plane in mW. The diameter of field of the view (FOV) was then calculated by dividing the objective lens field number (FN) by its magnification. For the Klaus 60x lens, the FN is $26.5\ mm$. The value of the diameter of the FOV was then used to calculate the area of field of view in mm^2. Finally, the irradiance (I) is given by

$$I = \frac{Power}{Area}. \qquad 1$$

The irradiance value of $15.99\ \mu W/mm^2$ was used for all the other experiments except when the irradiance was specifically varied (Fig. 2D).

Data availability

Raw and analysed data that support the findings of this study are available from the Lead contact (t.a.waigh@manchester.ac.uk) upon request.

Bacterial strain availability

Strains and further information should also be directed to the Lead contact, Thomas Waigh (t.a.waigh@manchester.ac.uk).

References

1. Kassinger, S. J. & van Hoek, M. L. Biofilm architecture: An emerging synthetic biology target. *Synth Syst Biotechnol* **5**, 1 (2020).

2. Sharma, G. *et al.* Escherichia coli biofilm: development and therapeutic strategies. *J Appl Microbiol* **121**, 309–319 (2016).

3. Prindle, A. *et al.* Ion channels enable electrical communication in bacterial communities. *Nature* **527**, 59–63 (2015).

4. Whitehead, N. A., Barnard, A. M. L., Slater, H., Simpson, N. J. L. & Salmond, G. P. C. Quorum-sensing in Gram-negative bacteria. *FEMS Microbiol Rev* **25**, 365–404 (2001).

5. Blee, J. A., Roberts, I. S. & Waigh, T. A. Spatial propagation of electrical signals in circular biofilms: A combined experimental and agent-based fire-diffuse-fire study. *Phys Rev E* **100**, 1–9 (2019).

6. Martinez-Corral, R., Liu, J., Süel, G. M. & Garcia-Ojalvo, J. Bistable emergence of oscillations in growing Bacillus subtilis biofilms. *Proc Natl Acad Sci U S A* **115**, 8333–8340 (2018).

7. Blee, J. A., Roberts, I. S. & Waigh, T. A. Membrane potentials, oxidative stress and the dispersal response of bacterial biofilms to 405 nm light. *Phys Biol* **17(3)**, 1–10 (2020).

8. Kharkwal, G. B., Sharma, S. K., Huang, Y. Y., Dai, T. & Hamblin, M. R. Photodynamic Therapy for Infections: Clinical Applications. *Lasers Surg Med* **43**, 755 (2011).

9. Cieplik, F. *et al.* Antimicrobial photodynamic therapy - what we know and what we don't. *Crit Rev Microbiol* **44**, 571–589 (2018).

10. Bruni, G. N., Weekley, R. A., Dodd, B. J. T. & Kralj, J. M. Voltage-gated calcium flux mediates Escherichia coli mechanosensation. *Proc Natl Acad Sci U S A* **114**, 9445–9450 (2017).

11. Martinac, B., Saimi, Y. & Kung, C. Ion Channels in Microbes. *Physiol Rev* **88**, 1449–1490 (2008).

12. Mackinnon, R. Potassium Channels and the Atomic Basis of Selective Ion Conduction. *Angew Int Ed. Engl* **43**, 75–100 (2004).

13. Yang, C. Y. *et al.* Encoding Membrane-Potential-Based Memory within a Microbial Community. *Cell Syst* **10**, 417–423 (2020).

14. Mishra, R. *et al.* Natural Anti-biofilm Agents: Strategies to Control Biofilm-Forming Pathogens. *Front Microbiol* **11**, 2640–2663 (2020).

15. Bruni, G. N. & Kralj, J. M. Membrane voltage dysregulation driven by metabolic dysfunction underlies bactericidal activity of aminoglycosides. *Elife* **9**, 1–25 (2020).

16. Kralj, J. M., Hochbaum, D. R., Douglass, A. D. & Cohen, A. E. Electrical Spiking in 'Escherichia coli' Probed with a Fluorescent Voltage-Indicating. *Source: Science, New Series* **333**, 345–348 (2011).

17. Milkman, R. An Escherichia coli homologue of eukaryotic potassium channel proteins. *Proc. Natd. Acad. Sci. USA* **91**, 3510–3514 (1994).

18. Kuo, M. M. C., Saimi, Y. & Kung, C. Gain-of-function mutations indicate that Escherichia coli Kch forms a functional K+ conduit in vivo. *EMBO J* **22**, 4049 (2003).

19. Beagle, S. D. & Lockless, S. W. Unappreciated Roles for K + Channels in Bacterial Physiology The Importance of K + for Cellular Functions. *Trends Microbiol* **29**, 942–950 (2021).

20. Biancalana, M. & Koide, S. Molecular mechanism of Thioflavin-T binding to amyloid fibrils. *Biochimica et Biophysica Acta - Proteins and Proteomics* vol. 1804 1405–1412 Preprint at (2010).

21. Plášek, J. & Sigler, K. Slow fluorescent indicators of membrane potential: a survey of different approaches to probe response analysis. *J Photochem Photobiol B* **33**, 101–124 (1996).

22. Stratford, J. P. *et al.* Electrically induced bacterial membrane-potential dynamics correspond to cellular proliferation capacity. *Proc Natl Acad Sci U S A* **116**, 9552–9557 (2019).

23. Humphries, J. *et al.* Species-Independent Attraction to Biofilms through Electrical Signaling. *Cell* **168**, 200–209 (2017).

24. Perry, S. W., Norman, J. P., Barbieri, J., Brown, E. B. & Gelbard, H. A. Mitochondrial membrane potential probes and the proton gradient: a practical usage guide. *Biotechniques* **50**, 98–115 (2011).

25. Buzsáki, G. *Rhythms of the Brain*. *Rhythms of the Brain* (Oxford University Press, UK., 2009).

26. Milkman, R. An Escherichia coli homologue of eukaryotic potassium channel proteins. *Proc Natl Acad Sci U S A* **91**, 3510–3514 (1994).

27. Loukin, S. H. *et al.* Microbial K+ channels. *Journal of General Physiology* **125**, 521–527 (2005).

28. Kuo, M. M. C., Haynes, W. J., Loukin, S. H., Kung, C. & Saimi, Y. Prokaryotic K(+) channels: from crystal structures to diversity. *FEMS Microbiol Rev* **29**, 961–985 (2005).

29. Baba, T. *et al.* Construction of Escherichia coli K-12 in-frame, single-gene knockout mutants: the Keio collection. *Mol Syst Biol* **2**, 1–10 (2006).

30. Herman, J. P. Neural control of chronic stress adaptation. *Front Behav Neurosci* **7**, 1–12 (2013).

31. Avery, S. N. *et al.* Stable habituation deficits in the early stage of psychosis: a 2-year follow-up study. *Translational Psychiatry 2021 11:1* **11**, 1–10 (2021).

32. Wu, Z. *et al.* A Habituation Sensory Nervous System with Memristors. *Advanced Materials* **32**, 1–6 (2020).

33. Martinez-Corral, R., Liu, J., Prindle, A., Süel, G. M. & Garcia-Ojalvo, J. Metabolic basis of brain-like electrical signalling in bacterial communities. *Philosophical Transactions of the Royal Society B: Biological Sciences* **374**, (2019).

34. Liu, J. *et al.* Coupling between distant biofilms and emergence of nutrient time-sharing. *Science (1979)* **356**, 638–642 (2017).

35. Li, Y., Moe, P. C., Chandrasekaran, S., Booth, I. R. & Blount, P. Ionic regulation of MscK, a mechanosensitive channel from Escherichia coli. *EMBO J* **21**, 5323–5330 (2002).

36. Booth, I. R. Bacterial mechanosensitive channels: progress towards an understanding of their roles in cell physiology. *Curr Opin Microbiol* **18**, 16 (2014).

37. Haswell, E. S., Phillips, R. & Rees, D. C. Mechanosensitive channels: what can they do and how do they do it? *Structure* **19**, 1356 (2011).

38. Martinac, B., Saimi, Y. & Kung, C. Ion channels in microbes. *Physiol Rev* **88**, 1449 (2008).

39. Van Den Berg, J., Galbiati, H., Rasmussen, A., Miller, S. & Poolman, B. On the mobility, membrane location and functionality of mechanosensitive channels in Escherichia coli. *Scientific Reports 2016 6:1* **6**, 1–11 (2016).

40. Gorochowski, T. E., Matyjaszkiewicz, A., Todd, T., Oak, N. & Kowalska, K. BSim: An Agent-Based Tool for Modeling Bacterial Populations in Systems and Synthetic Biology. *PLoS One* **7**, 1–10 (2012).

41. Alves, S. B. *et al.* Characterization of diffusion processes: Normal and anomalous regimes. *Physica A: Statistical Mechanics and its Applications* **447**, 392–401 (2016).

42. Woringer, M., Izeddin, I., Favard, C. & Berry, H. Anomalous Subdiffusion in Living Cells: Bridging the Gap Between Experiments and Realistic Models Through Collaborative Challenges. *Front Phys* **8**, 134–143 (2020).

43. Keener, J. & Sneyd, J. Wave propagation in higher dimensions. in *Mathematical Physiology I: Cellular Physiology* 257–262 (Springer, New York, NY., 2009).

44. Wussling, M. H. P. & Salz, H. Nonlinear propagation of spherical calcium waves in rat cardiac myocytes. *Biophys J* **70**, 1144–1153 (1996).

45. Lipp, P. & Niggli, E. Microscopic spiral waves reveal positive feedback in subcellular calcium signaling. *Biophys J* **65**, 2272–2276 (1993).

46. Wier, W. G. & Blatter, L. A. Ca2+-oscillations and Ca2+-waves in mammalian cardiac and vascular smooth muscle cells. *Cell Calcium* **12**, 241–254 (1991).

47. Nagy-Ungvarai, Z., Ungvarai, J., Müller, S. C. & Hess, B. The role of curvature and pulse width for transition to unstable wave fronts in the Belousov–Zhabotinsky reaction. *J Chem Phys* **97**, 1004–1009 (1998).

48. Liu, J. *et al.* Metabolic co-dependence gives rise to collective oscillations within biofilms. *Nature* **523**, 550–554 (2015).

49. Keener J & Sneyd J. *Mathematical Physiology I: Cellular Physiology*. (Springer, New York, NY., 2009).

50. Rooney, L. M., Amos, W. B., Hoskisson, P. A. & McConnell, G. Intra-colony channels in E. coli function as a nutrient uptake system. *ISME J* **14**, 2461 (2020).

51. Wilson, B. C. & Patterson, M. S. The physics, biophysics and technology of photodynamic therapy. *Phys Med Biol* **53**, 61–109 (2008).

52. Abana, C. M. *et al.* Characterization of blue light irradiation effects on pathogenic and nonpathogenic Escherichia coli. *Microbiologyopen* **6**, 1–10 (2017).

53. Mittler, R. Oxidative stress, antioxidants and stress tolerance. *Trends Plant Sci* **7**, 405–410 (2002).

54. Levitan, I. K. L. Learning and Memory. in *The Neuron: Cell and Molecular Biology* 537–588 (Oxford University Press, UK., 2002).

55. Kim, J. S., Chowdhury, N., Yamasaki, R. & Wood, T. K. Viable but non-culturable and persistence describe the same bacterial stress state. *Environ Microbiol* **20**, 2038–2048 (2018).

56. Marasini, S., Leanse, L. G. & Dai, T. Can microorganisms develop resistance against light based anti-infective agents? *Adv Drug Deliv Rev* **175**, 1–8 (2021).

57. Hennes, M., Bender, N., Cronenberg, T., Welker, A. & Maier, B. Collective polarization dynamics in bacterial colonies signify the occurrence of distinct subpopulations. *PLoS Biol* **21**, (2023).

58. Benarroch, J. M. & Asally, M. The Microbiologist's Guide to Membrane Potential Dynamics. *Trends in Microbiology* (2020).

59. Yu, R., Zhang, H. & Guo, B. Conductive Biomaterials as Bioactive Wound Dressing for Wound Healing and Skin Tissue Engineering. *Nanomicro Lett* **14**, (2022).

60. Jin, X. *et al.* Sensitive bacterial Vm sensors revealed the excitability of bacterial Vm and its role in antibiotic tolerance. *Proc Natl Acad Sci U S A* **120**, (2023).

61. Huang, C.-T., Peretti, S. W. & Bryers', J. D. Effects of Medium Carbon-to-Nitrogen Ratio on Biofilm Formation and Plasmid Stability. *Biotechnology Bioeng.* **44**, 329–336 (1993).

62. Soleimani, S., Ormeci, B. & Isgor, O. B. Growth and characterization of Escherichia coli DH5α biofilm on concrete surfaces as a protective layer against microbiologically influenced concrete deterioration (MICD). *Appl Microbiol Biotechnol* **97**, 1093–1102 (2013).

63. Jayaraman, A., Earthman, J. C. & Wood, T. K. Corrosion inhibition by aerobic biofilms on SAE 1018 steel. *Applied Microbiology and Biotechnology 1997 47:1* **47**, 62–68 (1997).

64. Hartmann, R. *et al.* Quantitative image analysis of microbial communities with BiofilmQ. *Nature Microbiology 2021 6:2* **6**, 151–156 (2021).

65. Wucher, B. R., Elsayed, M., Adelman, J. S., Kadouri, D. E. & Nadell, C. D. Bacterial predation transforms the landscape and community assembly of biofilms. *Curr Biol* **31**, 2643–2651 (2021).

66. Díaz-Pascual, F. *et al.* Breakdown of Vibrio cholerae biofilm architecture induced by antibiotics disrupts community barrier function. *Nature Microbiology* **4**, 2136–2145 (2019).

Acknowledgments

E.A. would like to thank Marie Goldrick for her assistance. E.A. would like to thank the Knut Drescher group for useful discussions on the use of BiofilmQ. E.A. would like to thank Johanna Blee, Raveen Tank, Emma Layton and Dan Han for useful discussions. The authors would like to thank the Prindle group for providing their code. Special thanks goes to Peter March, Roger Meadows and Steven Marsden for their help with the microscopy. The Bioimaging Facility microscopes used in this study were purchased with grants from the BBSRC, Welcome Trust and the University of Manchester Strategic Fund. R. K. is supported by the UKRI Future Leaders fellowship (MR/T021225/1). The authors would like to thank TETFund Nigeria and Abia State University Nigeria for E. A.'s PhD scholarship.

Authors contributions

E. A., T. W., and I. R. conceptualized and designed the experiments. E. A. performed all experiments including strain generation. E. A. performed all microscopy, image and data analysis. E. A. wrote the manuscript with input from all authors. R. K. contributed to the design of the microfluidic technique. E. A., T. W. and V. M. developed the models. E. A. and V. M. performed the simulations.

Competing interests

The authors declare no competing interests.